Research Article

Effect of Heat Treatment on the Microstructure and Corrosion Resistance of Stainless/Carbon Steel Bimetal Plate

Hao Li, Liyuan Zhang, Boyang Zhang, and Qingdong Zhang [ID]

School of Mechanical Engineering, University of Science and Technology Beijing, Beijing 100083, China

Correspondence should be addressed to Qingdong Zhang; b20160237@xs.ustb.edu.cn

In order to research the effect of heat treatment on the microstructure and corrosion resistance of stainless/carbon steel bimetal plate, the annealing process at 700°C with different times was carried out for stainless/carbon steel bimetal plate. Because the carbon content of carbon steel was higher than that of stainless steel, the carbon would diffuse from carbon steel to stainless steel in the bimetal plate during the annealing process. The carbon diffusion would cause the thickness of the decarburized layer in carbon steel and the carbon content of stainless steel to increase. The carbon diffusion would be ongoing with the annealing process until the carbon content of stainless steel reached 0.08%. The higher carbon content could help in the formation of more chromium-depleted regions in the stainless steel surface, causing the stainless steel in the bimetal plate to have a poorer surface corrosion resistance than that of stainless steel under the same annealing conditions.

1. Introduction

Due to its good mechanical properties and excellent corrosion resistance, type 304 austenitic stainless steel is one of the most widely utilized ferrous materials in many engineering fields [1, 2]. Nowadays, with the development of science and technology, stainless/carbon steel bimetal plate, as a substitute for stainless steel, has become increasingly popular for many engineering applications.

Stainless/carbon steel bimetal plate is a kind of metal composite plate which is comprised of stainless steel as the cladding and carbon steel as the substrate [3, 4]. Not only does stainless/carbon steel bimetal plate have good ductility and thermal conductivity from the carbon steel, but it also has high corrosion resistance and glossy appearance from the stainless steel [5, 6]. Furthermore, 304 stainless steel contains a lot of precious alloy elements and has a complex production process, which makes its cost very high. Using a stainless/carbon steel bimetal plate instead of stainless steel can save on production costs and materials greatly [7, 8]. Up to now, various technologies can be utilized to produce stainless/carbon steel bimetal plate, for instance, explosion welding [9],

diffusion bonding [10], and hot rolling bonding [11]. Among these, hot rolling is the main production method.

However, under some conditions, stainless steel could also be corroded [12, 13]. When 304 stainless steel is exposed to the temperature range of 550–850°C, the carbide will precipitate on the grain boundaries, forming the chromium-depleted region, which is susceptible to attack in a corrosive medium. When a large number of chromium-depleted regions appear, the corrosion resistance of the stainless steel would deteriorate [14, 15].

In view of this, some corrosion tests are usually carried out to evaluate the corrosion resistance of stainless steel [16, 17]. Similarly, the stainless/carbon steel bimetal plate will be no exception. For example, Murkute et al. used powder bed fusion-selective laser melting to fabricate 316L stainless steel/carbon steel clad plate, and they found that the proper process parameters could not only increase the bonding strength, but also improve the surface corrosion resistance of cladding [18]. Argade et al. achieved solid-state cladding of austenitic stainless steel on carbon steel substrate through friction stir lap welding process, and they showed the stainless steel lap welded/cladded surface showed similar

electrochemical characteristics as the base stainless steel in 3.5 wt.% NaCl solution [19].

However, for stainless/carbon steel bimetal plate, the effect of element diffusion should also be taken into consideration in the study of its corrosion resistance evolution. Many previous works have shown that there is a diffusion area with a certain thickness between the stainless steel and carbon steel, which makes the stainless steel and carbon steel bond together well [20]. Wang et al. investigated the effect of rolling reduction ratios on the microstructure, mechanical properties, and interface bonding mechanism of hot-rolled stainless steel clad plates, and they found that increasing the rolling deformation could increase the alloy element diffusion distance and the shear strength of clad plate [21]. Dhib et al. researched the mechanical bonding properties and interfacial morphologies of austenitic stainless steel clad plates, and they reported that the carbon diffusion between carbon steel and stainless steel changed the microstructure near the interface of clad plate [22]. At room temperature, the microstructure of the bimetal plate is stable and no element diffusion is observed. However, if element diffusion occurs in the bimetal plate within the temperature range of 550–850°C, it would affect the formation of chromium-depleted region in the stainless steel, subsequently influencing the surface corrosion resistance of the bimetal plate.

To our knowledge, few studies have reported on this aspect of bimetal plate. In view of this, in this paper, the effect of heat treatment at the temperature range of 700°C on the surface corrosion resistance of bimetal plate would be investigated, and the element diffusion in the bimetal plate during the heat treatment process would be researched; further, the relationship between the above two would also be studied. Investigating the evolution of microstructure and corrosion resistance of stainless/carbon steel bimetal plate at the high-temperature condition could be helpful to improve the heat treatment process of the bimetal plate.

2. Materials and Methods

In this paper, the bimetal plate was fabricated by hot rolling bonding, with carbon steel as the substrate and stainless steel as the cladding. The chemical compositions are shown in Table 1, which is analysed by the optical emission spectroscopy. The surfaces of the stainless steel and carbon steel were cleaned before rolling to remove contaminants and the oxide layer. The stainless steel was stacked with the carbon steel, and the edges of the plate were sealed through welding, with carbon steel as a wedge. Then, the air in the interface between the stainless steel and carbon steel was pumped out by a vacuum pump to reach the proper vacuum degree (0.5–5 Pa). The bimetal plate was rolled multiple times after being annealed in a pit furnace at 1050°C for 3 hours. The thicknesses of the carbon steel and stainless steel in the bimetal plate were 3 mm and 2 mm, respectively. The mechanical properties (the minimum tensile strength and minimum yield strength of the bimetal plate is greater than 485 MPa and 275 MPa, respectively) and bond quality (no single unbonded area exceeding 25 mm in its longest dimension with total unbonded area not exceeding 1% of the total cladded surface area) satisfied the ASTM A264-12 standard [23].

In this paper, two kinds of samples were annealed, Sample I and Sample II, as shown in Figure 1. Sample I was the stainless/carbon steel bimetal plate, and Sample II was the stainless steel cut from the cladding of the bimetal plate, which had a thickness of 1.5 mm. This paper would research and compare the surface corrosion resistance of the above two kinds of samples and would discuss the effect of substrate (carbon steel) with a carbon content of 0.173% on the corrosion resistance and microstructure of cladding (stainless steel).

Sample I and Sample II were annealed for 2 hours, 4 hours, 6 hours, and 8 hours, respectively, under a vacuum environment at 700°C (a total of five samples were annealed for each annealing condition). After annealing, the surface (test surfaces I and II as shown in Figure 1) corrosion resistance of all the samples (including the unannealed Sample I and Sample II) was researched by polarization test and electrochemical impedance spectroscopy (EIS). The polarization tests were conducted in 3.5% NaCl solution (before the test, N_2 gas was purged into the solution for 30 min to remove the dissolved oxygen) at a scan rate of 1 mV/s. A saturated Ag/AgCl electrode and a platinum electrode were used as the reference and counterelectrode, respectively. The EIS measurements were performed under 5 mV amplitude of sinusoidal potential signals with respect to the open-circuit potential, over a frequency range from 100 kHz to 10 MHz.

The metallographic analysis and element distribution analysis were also carried out for the bimetal plate (Sample I) in this paper. The carbon steel was etched with 4% nitric acid alcohol solution, and the stainless steel was etched electrolytically with 10% oxalic acid water solution at 1 A/cm² for 1.5 min. As we know, carbon steel has a worse corrosion resistance than stainless steel, so carbon steel could be etched when stainless steel is ongoing metallographic corrosion, which could affect the microstructure observation of stainless steel. In view of this, the metallographic corrosion of stainless steel and carbon steel was conducted separately, and the carbon steel was removed by a low-concentration nitric acid solution before stainless steel was etched. After metallographic corrosion, the microstructure of the samples in the thickness direction was observed through a scanning electron microscope (SEM). The element distribution of the samples in the thickness direction was researched by an electron probe microanalyser (EPMA). Because the stainless steel (Sample II) was not affected by the other material (i.e., there was no element diffusion in stainless steel during the annealing process), the metallographic analysis and element distribution analysis were not carried out for the stainless steel (Sample II) in this paper.

3. Results and Discussion

Figure 2 shows the polarization curves of Sample I and Sample II. Table 2 gives the corresponding fitting values of the electrochemical parameters. In general, the corrosion potential (E_{corr}), the pitting potential (E_{pit}), and the

TABLE 1: Chemical composition of the stainless steel and carbon steel (wt.%).

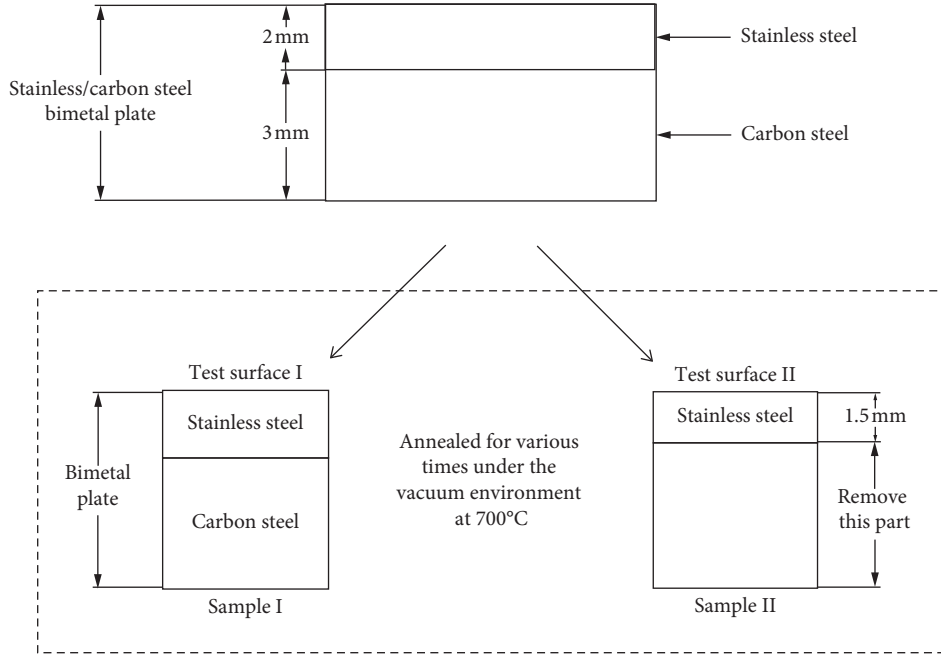| Elements	Cr	Ni	Mn	C	S	Si	P	Fe
304	17.892	8.032	1.958	0.042	0.019	0.805	0.025	Balance
Carbon steel	0	0	1.032	0.173	0.038	0.326	0.045	Balance

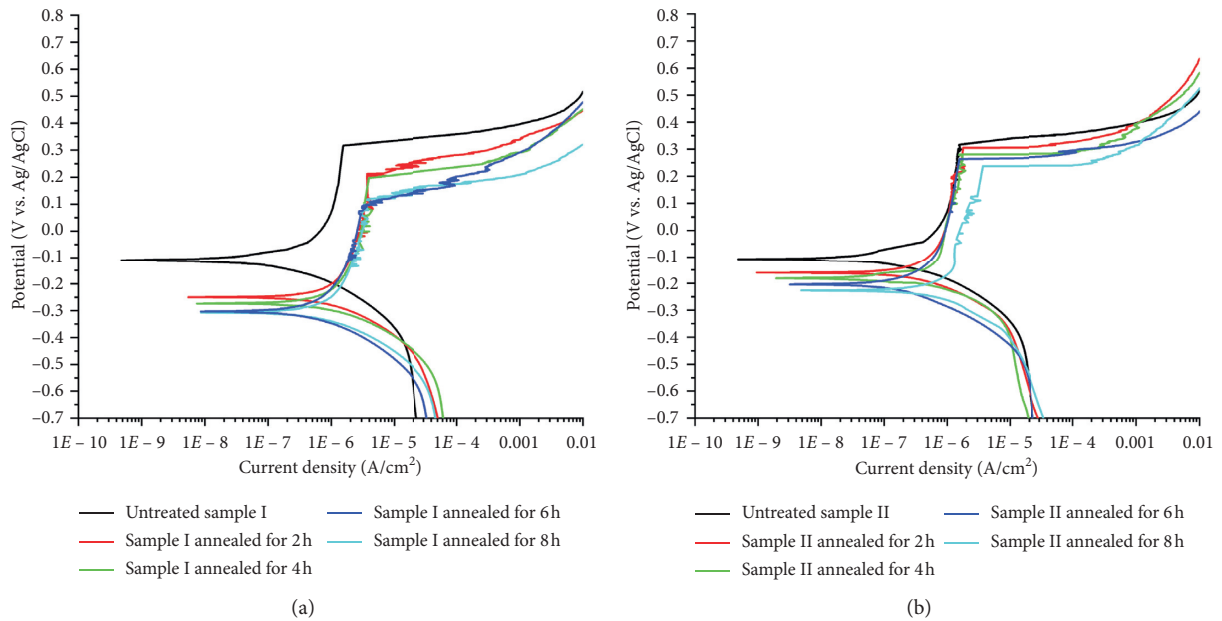FIGURE 1: Sampling schematic diagram for Sample I and Sample II.

FIGURE 2: Polarization curves of Sample I (a) and Sample II (b) with different annealing times.

corrosion current density (I_{corr}) are used to describe the active dissolution ability of materials. As shown in Figure 2 and Table 2 for the polarization curves, there was little difference between untreated Sample I and untreated Sample II, and their polarization curve fitting values were basically equal. As the annealing time increased, the E_{corr} values and E_{pit} values of both kinds of samples decreased, and the I_{corr} values of both kinds of samples increased. Compared with

TABLE 2: Polarization curve fitting results.

Sample	E_{corr} (V vs. Ag/AgCl)	I_{corr} (A/cm^2)	E_{pit} (V vs. Ag/AgCl)
Untreated Sample I	−1.050	1.48×10^{-7}	0.317
Sample I annealed for 2 h	−0.250	8.69×10^{-7}	0.213
Sample I annealed for 4 h	−0.273	1.08×10^{-6}	0.196
Sample I annealed for 6 h	−0.306	1.29×10^{-6}	0.109
Sample I annealed for 8 h	−0.303	1.32×10^{-6}	0.115
Untreated Sample II	−0.107	1.54×10^{-7}	0.317
Sample II annealed for 2 h	−0.160	2.89×10^{-7}	0.304
Sample II annealed for 4 h	−0.181	3.58×10^{-7}	0.280
Sample II annealed for 6 h	−0.204	4.65×10^{-7}	0.263
Sample II annealed for 8 h	−0.226	6.15×10^{-7}	0.237

Sample II, at the same annealing period, the E_{corr} values and E_{pit} values of Sample I were smaller, and the I_{corr} values of Sample I were larger. Furthermore, there was little difference in the E_{corr} value, E_{pit} value, and I_{corr} value for Sample I when annealed for 6 hours or 8 hours.

Figure 3 shows the Nyquist curves of Sample I and Sample II. It can be seen that, at the frequency range, every Nyquist curve is semicircular shaped. The untreated Sample I and untreated Sample II have basically the same curve radius, larger than that of the other samples. As the annealing time increases, the curve radius of both Sample I and Sample II decreases, which indicates that the impedance of both kinds of samples decreases as the annealing time increases. However, the impedance of Sample I is much smaller than that of Sample II at the same annealing period, and the difference in the curve radius of Sample I annealed for 6 hours or 8 hours is not large.

According to the features of EIS data, an equivalent electrical circuit of all the samples was established, as shown in Figure 4. R_s and R_t represent the electrolyte solution resistance and the charge transfer resistance, respectively. Q_{dl} represents the double-layer capacitance, and n is the parameter of Q_{dl} presenting the degree of surface inhomogeneity. As shown in Table 3, both the R_s value and Q_{dl} values of all the samples are basically equal, which indicates that the equivalent electrical circuit is reliable and stable. The R_t values of untreated Sample I and untreated Sample II were the largest among all the samples, and their values were very close at $3.553 \times 10^5 \, \Omega/cm^2$ and $3.538 \times 10^5 \, \Omega/cm^2$, respectively. The R_t values of Sample I annealed for 2 hours, 4 hours, 6 hours, and 8 hours were $2.370 \times 10^5 \, \Omega/cm^2$, $1.911 \times 10^5 \, \Omega/cm^2$, $1.758 \times 10^5 \, \Omega/cm^2$, and $1.721 \times 10^5 \, \Omega/cm^2$, respectively. Similarly, the R_t values of Sample II annealed for 2 hours, 4 hours, 6 hours, and 8 hours were $2.842 \times 10^5 \, \Omega/cm^2$, $2.670 \times 10^5 \, \Omega/cm^2$, $2.487 \times 10^5 \, \Omega/cm^2$, and $2.316 \times 10^5 \, \Omega/cm^2$, respectively. The R_t values of both Sample I and Sample II showed a decreasing trend with increasing annealing time, indicating that the corrosion resistance decreased gradually. However, the R_t value of Sample I was obviously smaller than that of Sample II at the same annealing period, and the R_t value difference between Sample I annealed for 6 hours and 8 hours was very small.

Based on the above analysis, the polarization curve results are in good agreement with the Nyquist curves and the equivalent electrical circuit results. The untreated Sample I and untreated Sample II have basically the same corrosion resistance; the corrosion resistance of both Sample I and Sample II decreased as the annealing time increased, but the corrosion resistance of Sample I decreased more than that of Sample II at the same annealing period; the corrosion resistance of Sample I annealed for 6 hours and 8 hours was basically unchanged. The above results show that, at room temperature, the substrate has no effect on the corrosion resistance of the cladding in the bimetal plate. However, at 700°C, the substrate affected the cladding somehow, decreasing the cladding corrosion resistance. In view of this, it is necessary to analyse the effect of cladding on the substrate through SEM and EMPA.

Figure 5 shows the microstructure of the carbon steel (substrate) of untreated Sample I in the thickness direction. The interface between carbon steel and stainless steel is clearly visible. According to different microstructures, carbon steel can be divided into two parts: the area away from the interface and the area near the interface (approximately 80 μm thick). The carbon steel in the area away from the interface is carbon steel, which is comprised of pearlite (the white structure) and ferrite; the area near the interface is comprised of ferrite with little pearlite. The loss of pearlite indicates the decline of carbon content in the area near the interface.

Figure 6 shows the microstructure of the stainless steel (cladding) of untreated Sample I in the thickness direction. According to the different microstructures, stainless steel can be divided into two parts: the area away from the interface and the area near the interface (approximately 150 μm thick). The stainless steel grains in the area near the interface were surrounded by corrosion grooves, as shown in Figure 6(b). However, there were no corrosion grooves in the area away from the interface, as shown in Figure 6(c). According to the ATSM A262-15 standard [24], the microstructure in the area near the interface and in the area away from the interface could be called ditch structures (one or more grains completely surrounded by ditches) and step structures (steps only between grains, no ditches at grain boundaries), respectively.

Figure 7 shows the major element content distribution in the thickness direction of the bimetal plate. As shown in Figure 7(a), the element content of Fe, Cr, Ni, and Mn remained basically unchanged in the carbon steel and stainless steel. However, between the stainless steel and carbon steel, there was an element transition layer with a thickness of 20 μm. In the layer, the element content of Fe, Cr, Ni, and Mn varied monotonically and linearly along the
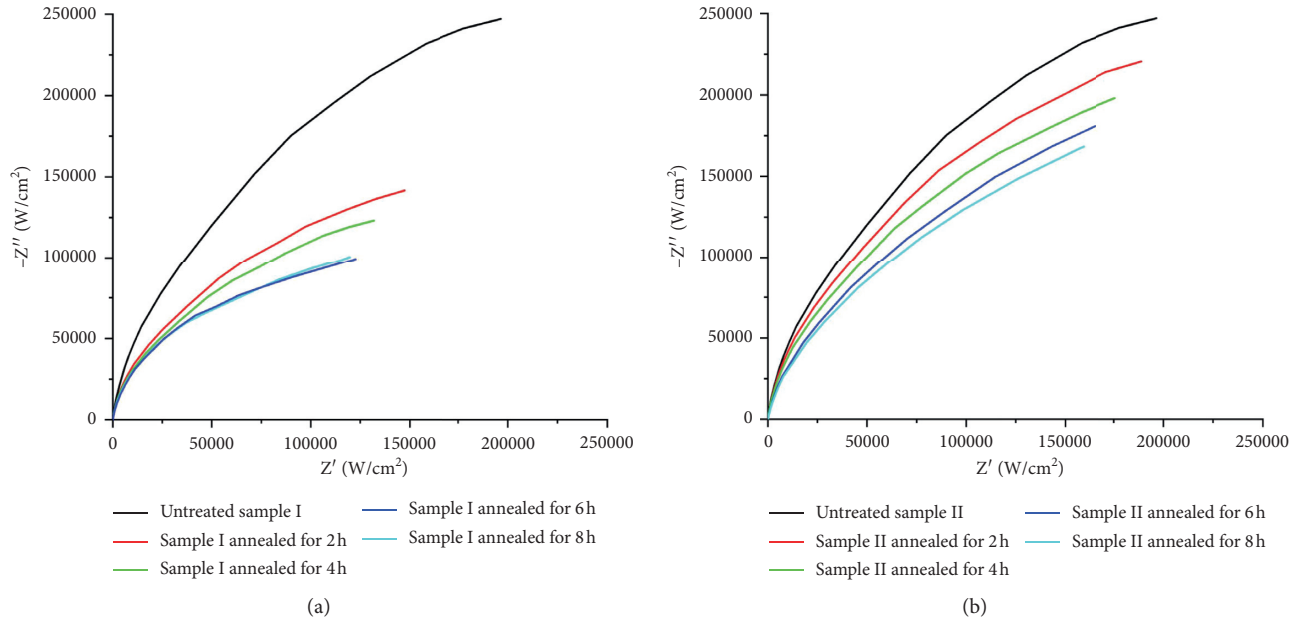
(a)

(b)

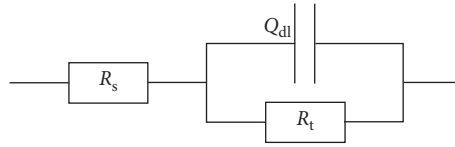FIGURE 3: Nyquist curves of Sample I (a) and Sample II (b) with different annealing times.

FIGURE 4: Equivalent electrical circuit for fitting the EIS experiment.

TABLE 3: Equivalent electrical circuit parameter fitted results.

Sample	R_s ($\Omega \cdot cm^{-2}$)	Q_{dl} ($\Omega^{-1} cm^{-2} \cdot s^{-n}$)	n	R_t ($\Omega \cdot cm^{-2}$)
Untreated Sample I	5.286	4.735×10^{-5}	0.91	3.553×10^5
Sample I annealed for 2 h	5.179	4.278×10^{-5}	0.90	2.370×10^5
Sample I annealed for 4 h	5.308	5.412×10^{-5}	0.91	1.911×10^5
Sample I annealed for 6 h	5.137	4.879×10^{-5}	0.89	1.758×10^5
Sample I annealed for 8 h	5.332	4.365×10^{-5}	0.90	1.721×10^5
Untreated Sample II	5.278	5.089×10^{-5}	0.89	3.538×10^5
Sample II annealed for 2 h	5.196	4.984×10^{-5}	0.89	2.842×10^5
Sample II annealed for 4 h	5.279	4.548×10^{-5}	0.91	2.670×10^5
Sample II annealed for 6 h	5.312	4.629×10^{-5}	0.90	2.487×10^5
Sample II annealed for 8 h	5.194	5.336×10^{-5}	0.90	2.316×10^5

thickness direction. The above element distribution does not correspond well to the different microstructures in Figures 5 and 6. As shown in Figure 7(b), according to the different carbon contents from the carbon steel side to stainless steel side, the carbon distribution can be divided into five parts: A area, B area (approximately 80 μm thick), C area (approximately 20 μm thick), D area (approximately 150 μm thick), and E area. The carbon contents of the A area, B area, D area, and E area are 0.16%, 0.12%, 0.10%, and 0.03%, respectively. Compared to the A area, the B area has a lower carbon content, which corresponds to the loss of pearlite in the area near the interface in Figure 5, and the A area corresponds to the area away from the interface, as shown in Figure 5.

According to the thickness, the D area and E area correspond to the area near the interface in Figure 6 and the area away from the interface in Figure 6, respectively. The carbon distribution in the thickness direction of the bimetal plate corresponds well to the different microstructures in Figures 5 and 6. The above results are in agreement with previous works reported by Dhib et al. and Jun et al. [25, 26]. In their papers, according to the different carbon contents, the B area, C area, and D area were called the decarburized layer, interface layer, and carburized layer, respectively. They believed that the formation of the decarburized layer and carburized layer was related to the carbon diffusion between the carbon steel and stainless steel in the bimetal plate.
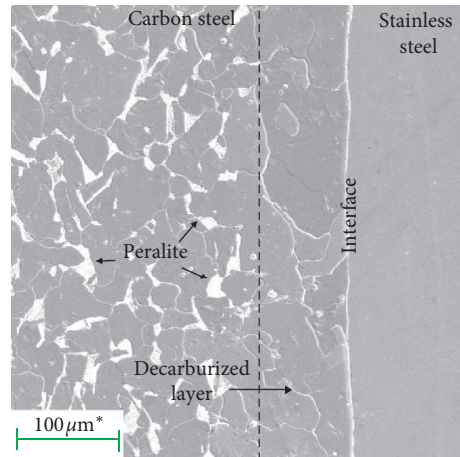
FIGURE 5: The microstructure in the thickness direction of the carbon steel (substrate) in the bimetal plate.
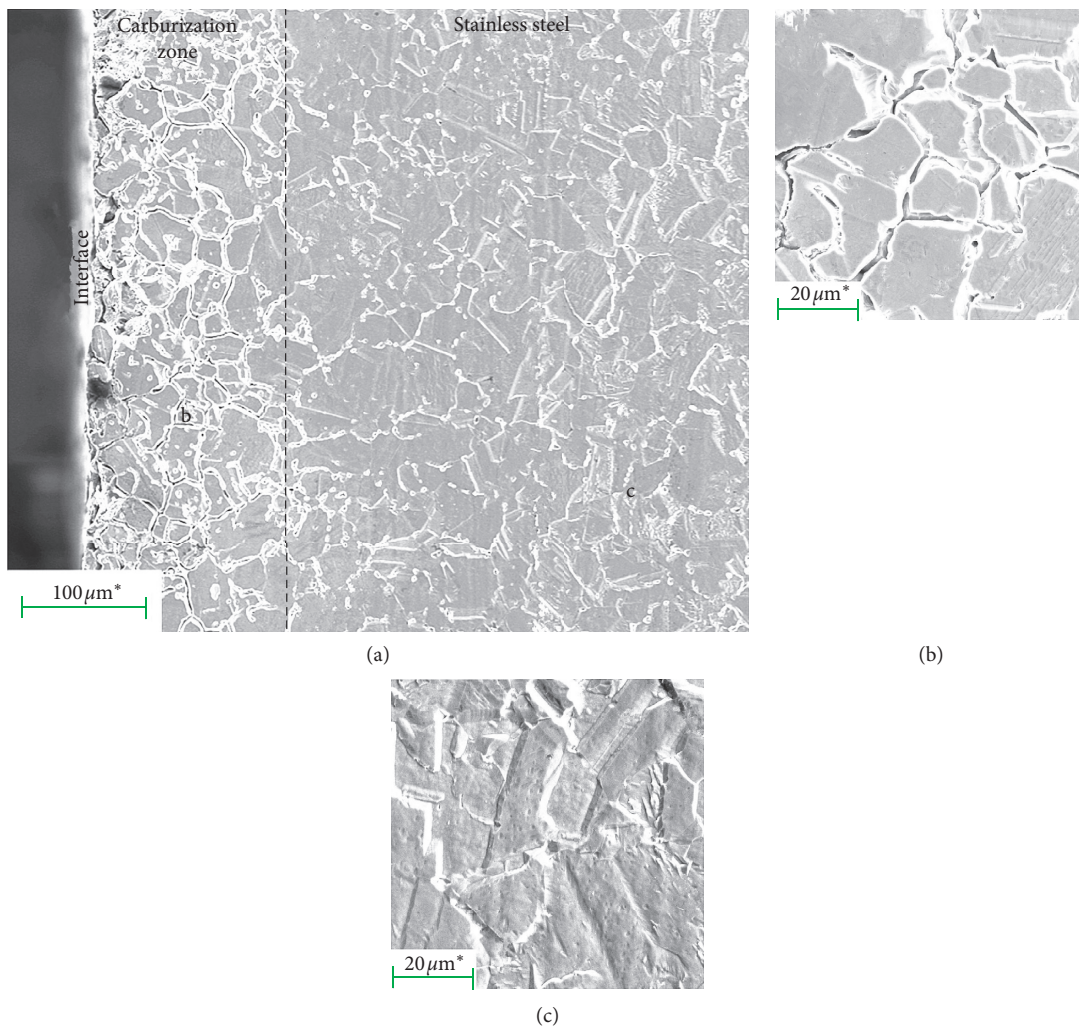

(a)

(b)

(c)

FIGURE 6: The microstructure in the thickness direction of stainless steel (cladding) in the bimetal plate: (a) macropicture and (b) and (c) micropicture.

Figure 8 shows the microstructure of carbon steel (substrate) in the bimetal plate at 700°C with different annealing times. As shown in Figure 8, there is little pearlite in the carbon steel, which is only comprised of ferrite, indicating that only the decarburized layer can be observed in Figure 8. Figure 9 shows the microstructure of stainless steel
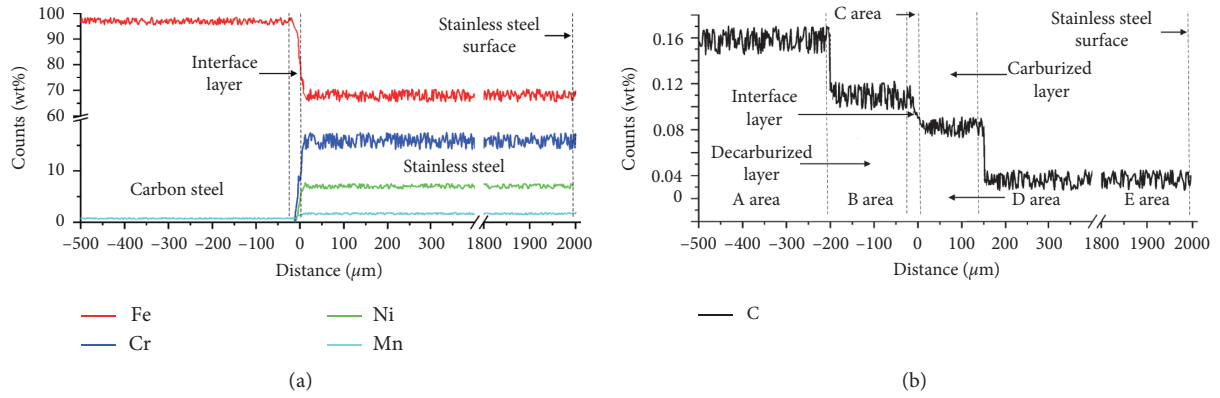
(a)

(b)

FIGURE 7: The element distribution in the thickness direction of the bimetal plate: (a) the element content of Fe, Cr, Ni, and Mn and (b) the element content of C.
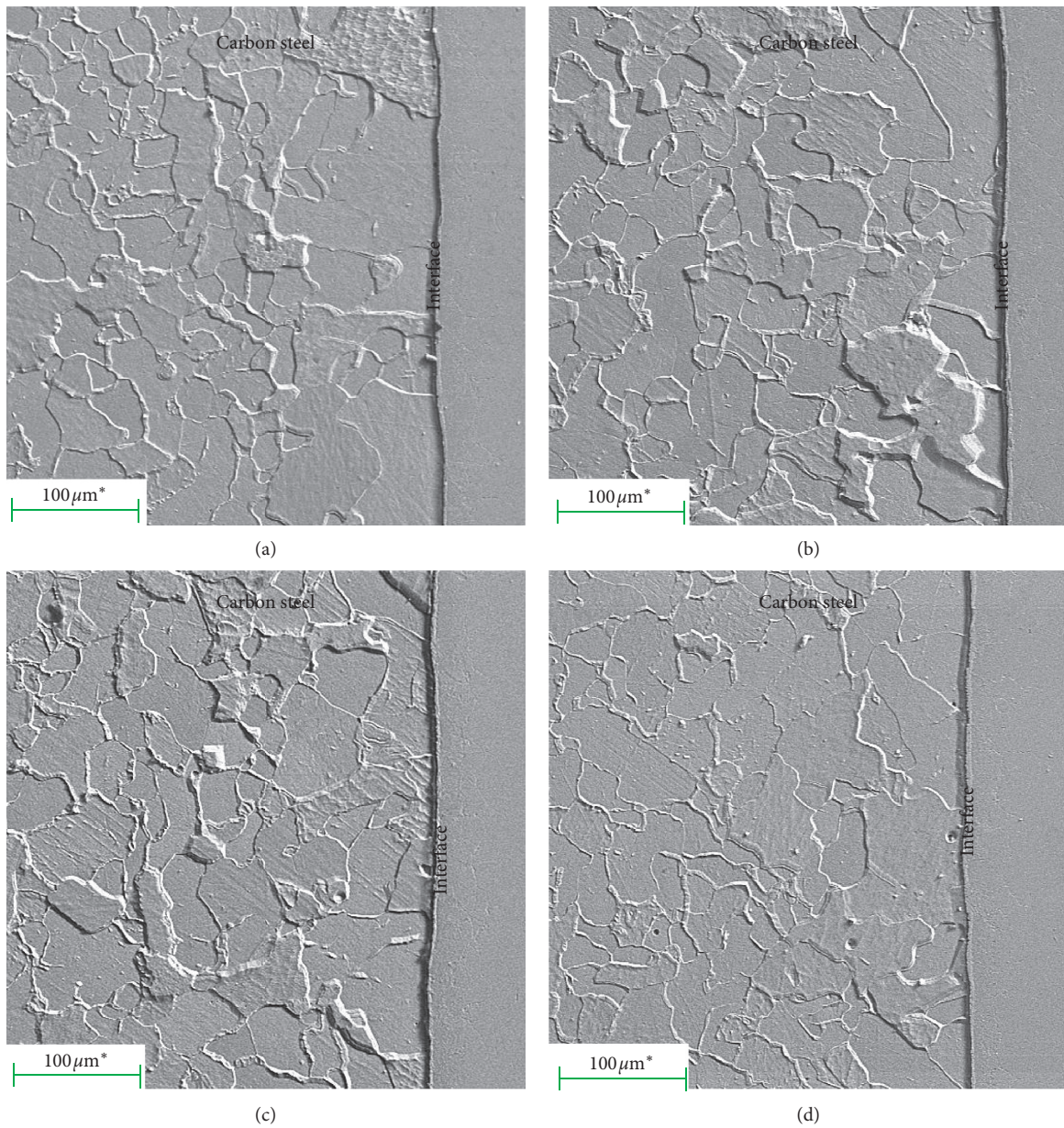

(a)

(b)

(c)

(d)

FIGURE 8: The microstructure in the thickness direction of carbon steel (substrate) in the bimetal plate at 700°C with different annealing times: (a) 2 h, (b) 4 h, (c) 6 h, and (d) 8 h.
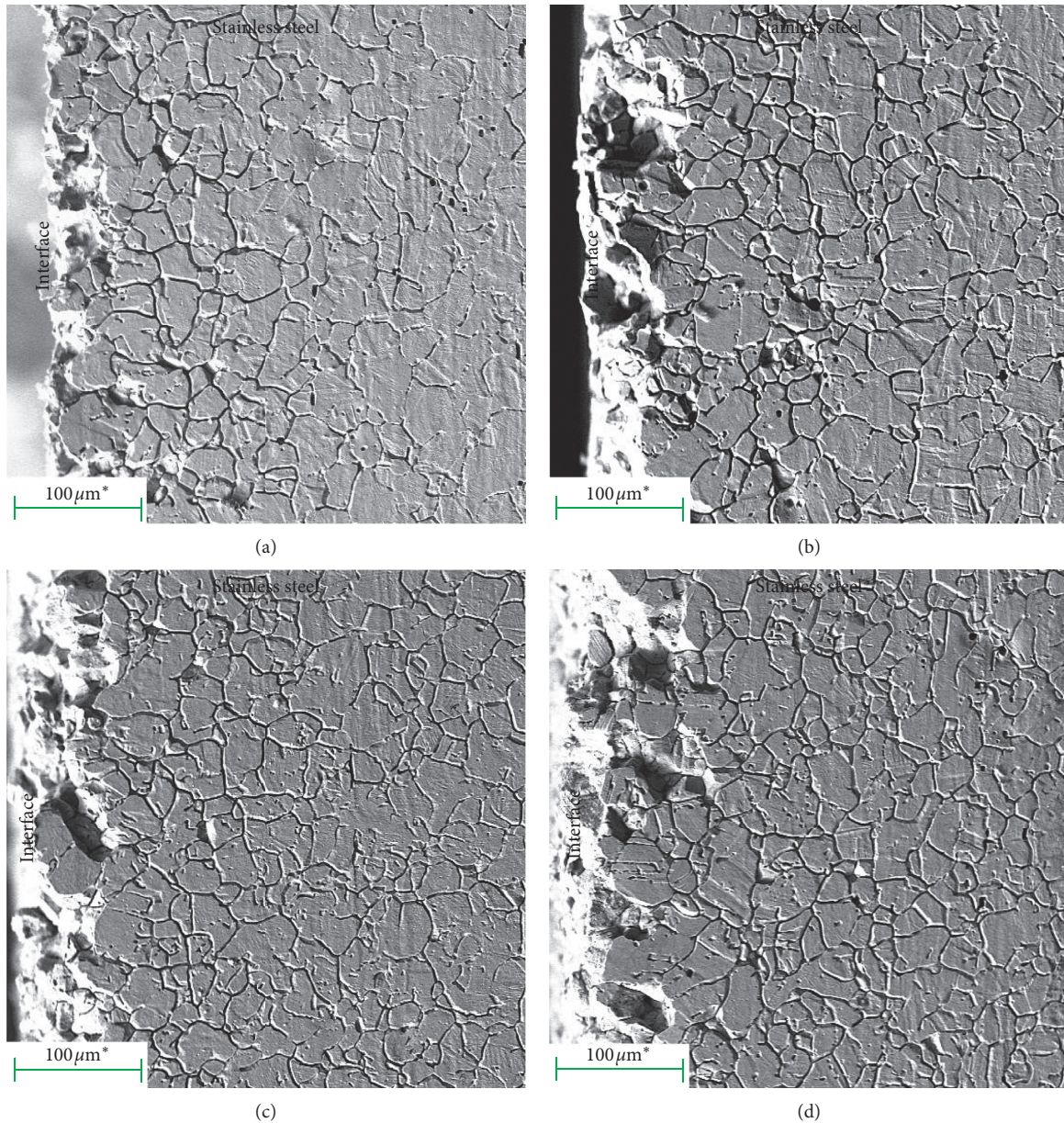
FIGURE 9: The microstructure in the thickness direction of stainless steel (cladding) in the bimetal plate at 700°C with different annealing times: (a) 2 h, (b) 4 h, (c) 6 h, and (d) 8 h.

(cladding) in the bimetal plate at 700°C with different annealing times. As shown in Figures 9(a) and 9(b), both the areas near the interface are ditch structures. However, unlike the area away from the interface in Figure 6, some ditches appear in the area away from the interface in Figures 9(a) and 9(b). Moreover, compared with Figure 9(a), there are more ditches in the area away from the interface in Figure 9(b). As shown in Figures 9(c) and 9(d), there is no step structure in the stainless steel. In these conditions, the carburized layer could not be differentiated from the stainless steel according to their metallographic features.

Figure 10 shows the element distribution of Fe, Cr, Ni, and Mn in the thickness direction of the bimetal plate at 700°C with different annealing times. It can be seen that the

element distributions of Fe, Cr, Ni, and Mn at 700°C with different annealing times are basically the same as those of the untreated sample at room temperature, which indicates that the annealing process did not affect the element distributions of Fe, Cr, Ni, and Mn in the bimetal plate.

Figure 11 shows the element distribution of C in the thickness direction of the bimetal plate at 700°C with different annealing times. The thickness of the interface layer remained unchanged during the annealing process. The thicknesses of the decarburized layer at 700°C annealed for 2 h, 4 h, 6 h, and 8 h were 520 μm, 750 μm, 980 μm, and 1010 μm, respectively. It can be seen that the thickness of the decarburized layer increased with the annealing time, but the thicknesses of the decarburized layer at 700°C annealed for
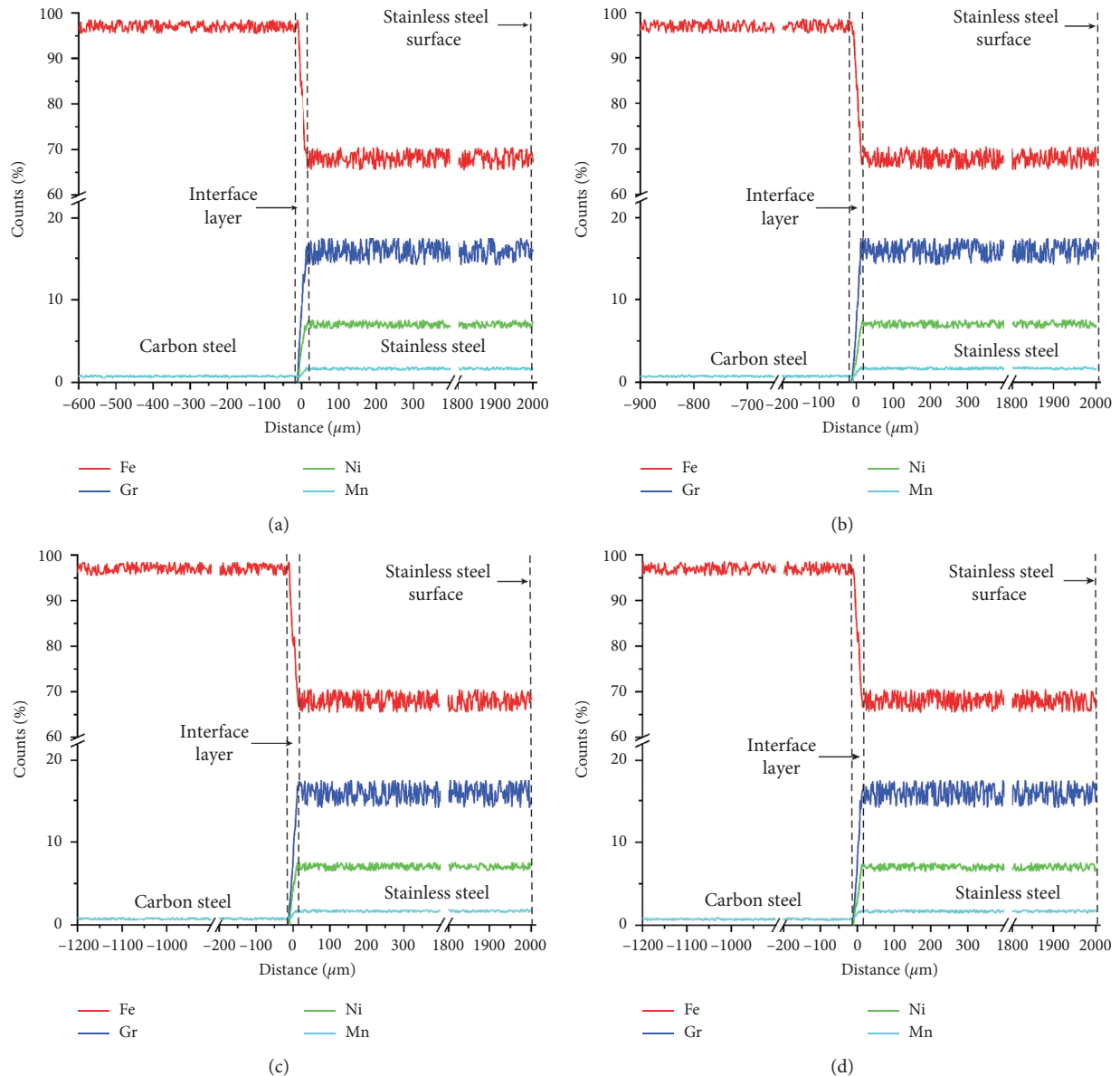
FIGURE 10: The element distribution of Fe, Cr, Ni, and Mn in the thickness direction of the bimetal plate at 700°C with different annealing times: (a) 2 h, (b) 4 h, (c) 6 h, and (d) 8 h.

6 h and 8 h were very close. The carbon contents of the stainless steel at 700°C annealed for 2 h, 4 h, 6 h, and 8 h were 0.05%, 0.06%, 0.08%, and 0.08%, respectively. The carbon content of the stainless steel at 700°C annealed for 6 h and 8 h was basically unchanged, and their carbon contents were equal with that of the carburized layer. In these conditions, the carburized layer could not be differentiated from the stainless steel by carbon content.

The above results show that, during the annealing process in the bimetal plate, the carbon diffusion between the stainless steel and carbon steel would occur, and the carbon diffusion would affect the surface corrosion resistance. Therefore, referring to previous research results, this paper proposes two models to illustrate corrosion behaviour during heat treatment of stainless steel and stainless/carbon steel bimetal plate [27, 28]. As shown in Figure 12, in

stainless steel, within the temperature range of 550–850°C, the carbon will diffuse gradually from grains to grain boundaries, combining with chromium on the grain boundaries to form carbides such as $M_{23}C_6$, causing a chromium-depleted region to appear on the grain boundaries. The chromium-depleted region enlarges as the annealing time increases, causing the surface corrosion resistance of stainless steel to decrease gradually [29, 30].

In this paper, the experimental results showed that the annealing process at 700°C would induce the carbon diffusion to occur between the carbon steel and stainless steel in the bimetal plate. The carbon diffusion would cause the thickness of the decarburized layer in the carbon steel and the carbon content of the stainless steel to increase. When the carbon content of the stainless steel reaches 0.08% (the original carbon content of the carburized layer), carbon
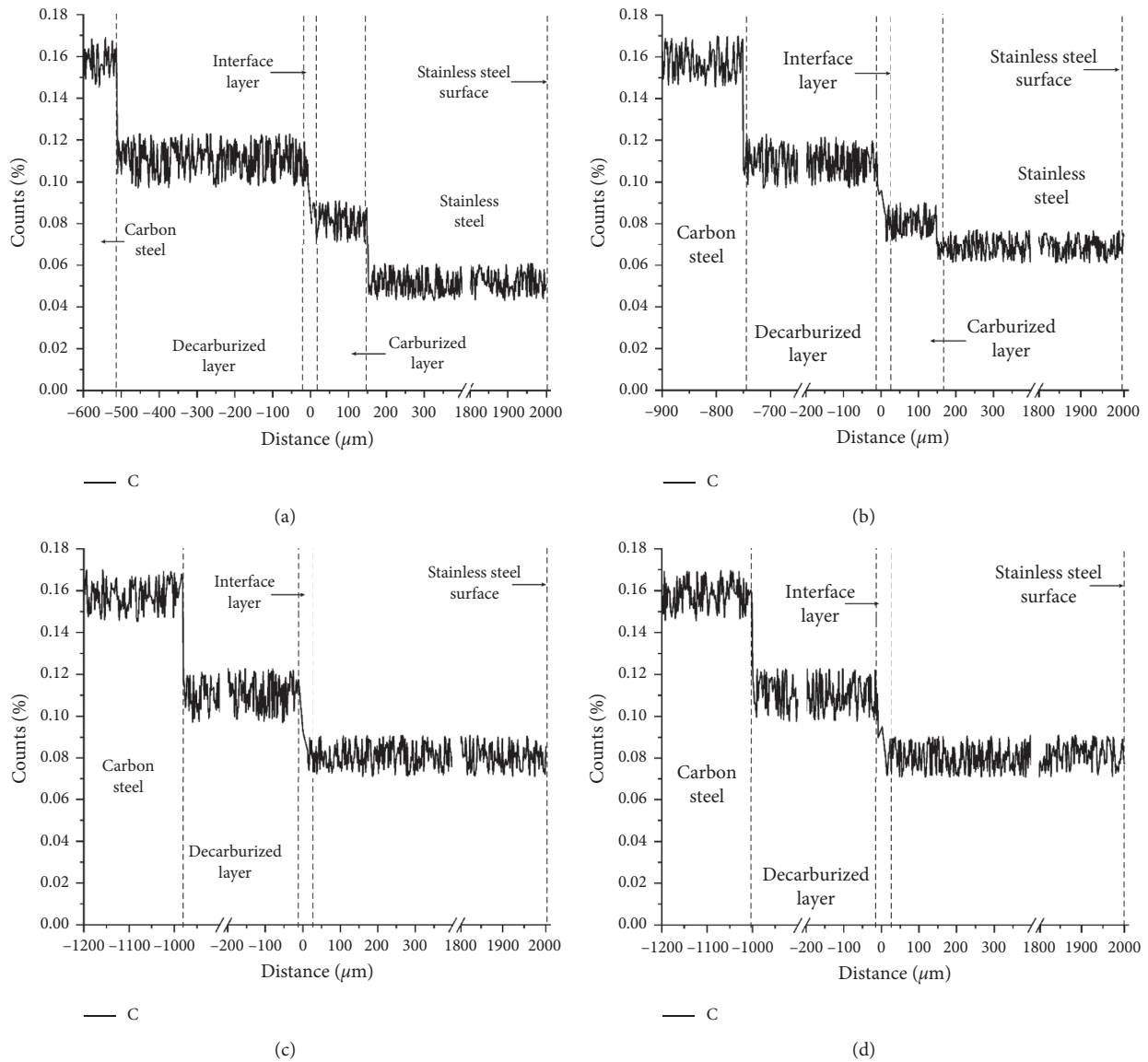
Figure 11: The element distribution of C in the thickness direction of the bimetal plate at 700°C with different annealing times: (a) 2 h, (b) 4 h, (c) 6 h, and (d) 8 h.
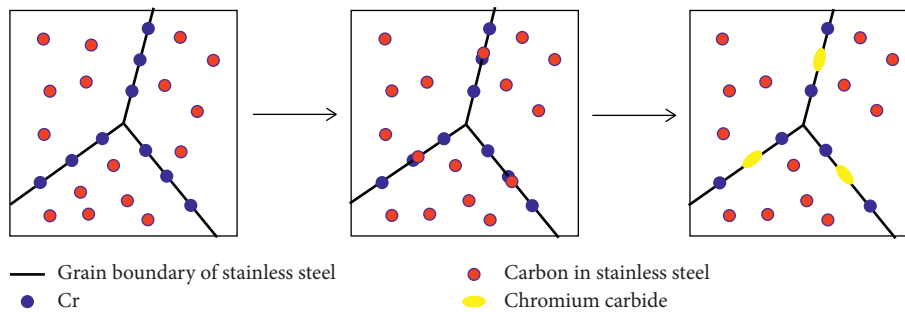

Figure 12: Schematic illustration of the formation of chromium-depleted region in stainless steel.

diffusion in the bimetal plate would stop. Many previous works have also reported on the carbon diffusion that occurs between stainless steel and carbon steel in the bimetal plate, and it is believed that the carburized layer in the bimetal

plate has a worse corrosion resistance than stainless steel. Through TEM and SAED analysis, Liu et al. found that there were carbides (mostly $M_{23}C_6$) on the grain boundaries of the carburized layer in the bimetal plate, and the carbon

— Grain boundary of stainless steel
● Cr
● Carbon in stainless steel
● Chromium carbide
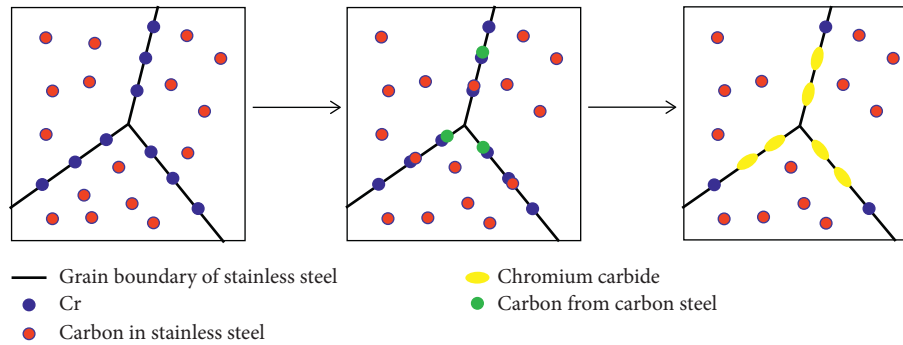● Carbon from carbon steel

FIGURE 13: Schematic illustration of the formation of chromium-depleted region in the stainless steel/carbon steel bimetal plate.

decrease made pearlite disappear from the decarburized layer in the bimetal plate [31, 32]. According to XRD and TEM results, Yu et al. revealed the carbon diffusion process between carbon steel and stainless steel in the bimetal plate and thought that carbon diffusion occurred during the manufacturing process of bimetal plate. They also proposed that, within the temperature range of 550–850°C, carbon diffusion could continue to occur in the bimetal plate [33]. The upper content limit of carbon in stainless steel should be related to the material properties of stainless steel and the diffusion activation energy of carbon, which require further research and discussion.

Therefore, the carbon diffusion between stainless steel and carbon steel in bimetal plate would affect the surface corrosion resistance of stainless steel in the bimetal plate. As shown in Figure 13, within the temperature range of 550–850°C, the carbon in the stainless steel will diffuse from the grains to grain boundaries, and the carbon in the carbon steel will also diffuse from the carbon steel to the stainless steel. The carbon from the two different areas combines with the chromium on the grain boundaries of the stainless steel to form carbides, making a chromium-depleted region appear on the grain boundaries of the stainless steel in the bimetal plate. Under the same conditions and at the same time point, compared with stainless steel, there would be more carbon to combine with chromium on the grain boundaries of the stainless steel in the bimetal plate, which would induce more chromium-depleted regions to appear, causing the stainless steel surface to have a worse corrosion resistance.

4. Conclusions

The microstructure and corrosion resistance of stainless/ carbon steel bimetal plate annealed at 700°C with different times were researched in this paper. The experimental results showed that, during the annealing process, as carbon steel had a higher carbon content than stainless steel, carbon diffusion from carbon steel to stainless steel would occur in bimetal plate, which could raise the thickness of the decarburized layer in carbon steel and increase the carbon content of the stainless steel. The carbon diffusion in bimetal plate would stop when the carbon content of the stainless steel reached 0.08%. With the increase of carbon content in the stainless steel, there would be more carbon to combine

with chromium on the grain boundaries of stainless steel and more chromium-depleted regions formed in the stainless steel surface, causing the stainless steel in the bimetal plate to have a poorer surface corrosion resistance than that of stainless steel under the same annealing conditions.

Data Availability

The test data used to support the findings of this study have been deposited in the Hindawi (Advance in Materials Science and Engineering) repository. The test data are included within the article and can be made freely available.

Conflicts of Interest

The authors declare no conflicts of interest.

Acknowledgments

References

[1] K. H. Lo, C. H. Shek, and J. K. L. Lai, "Recent developments in stainless steels," *Materials Science and Engineering: R: Reports*, vol. 65, no. 4-6, pp. 39–104, 2009.

[2] J. Z. Lu, W. W. Deng, K. Y. Luo, L. J. Wu, and H. F. Lu, "Surface EBSD analysis and strengthening mechanism of AISI304 stainless steel subjected to massive LSP treatment with different pulse energies," *Materials Characterization*, vol. 125, pp. 99–107, 2017.

[3] B. X. Liu, C. X. Chen, F. X. Yin et al., "Microstructure analysis and weldability investigation of stainless steel clad plate," *Energy Materials*, pp. 425–433, Springer, Cham, Switzerland, 2017.

[4] J. L. Xue, J. Bouchard, X. D. Chen, Z. C. Fan, and Y. Zhou, "Anisotropic elastic constants calculation of stainless steel cladded layers of pressure vessel steel plate," *Key Engineering Materials*, vol. 795, pp. 215–222, 2019.

[5] C. X. Chen, M. Y. Liu, and B. X. Liu, "Microstructures and tensile behaviors of stainless steel clad plate," in *Proceedings of Chinese Materials Conference*, Yinchuan, China, July 2017.

[6] W. Jiang, Y. Luo, G. Zhang, W. Woo, and S. T. Tu, "Experimental to study the effect of multiple weld-repairs on microstructure, hardness and residual stress for a stainless

steel clad plate," *Materials & Design*, vol. 51, pp. 1052–1059, 2013.

[7] Z. Zhu, Y. He, X. Zhang, H. Liu, and X. Li, "Effect of interface oxides on shear properties of hot-rolled stainless steel clad plate," *Materials Science and Engineering: A*, vol. 669, pp. 344–349, 2016.

[8] K. Kang, Y. Kawahito, M. Gao, and X. Zeng, "Effects of laser-arc distance on corrosion behavior of single-pass hybrid welded stainless clad steel plate," *Materials & Design*, vol. 123, pp. 80–88, 2017.

[9] R. Mendes, J. B. Ribeiro, and A. Loureiro, "Effect of explosive characteristics on the explosive welding of stainless steel to carbon steel in cylindrical configuration," *Materials & Design*, vol. 51, pp. 182–192, 2013.

[10] K. Meng, Y. Zhang, and Z.-W. Zhang, "Diffusion bonding of low carbon steel and pure zirconium with Cu-base amorphous interlayer," *Journal of Materials Processing Technology*, vol. 262, pp. 471–478, 2018.

[11] Z. Luo, G. Wang, G. Xie, L. Wang, and K. Zhao, "Interfacial microstructure and properties of a vacuum hot roll-bonded titanium-stainless steel clad plate with a niobium interlayer," *Acta Metallurgica Sinica (English Letters)*, vol. 26, no. 6, pp. 754–760, 2013.

[12] J. Xin, Y. Song, C. Fang, J. Wei, C. Huang, and S. Wang, "Evaluation of inter-granular corrosion susceptibility in 316LN austenitic stainless steel weldments," *Fusion Engineering and Design*, vol. 133, pp. 70–76, 2018.

[13] G. H. Aydoğdu and M. K. Aydinol, "Determination of susceptibility to intergranular corrosion and electrochemical reactivation behaviour of AISI 316L type stainless steel," *Corrosion Science*, vol. 48, no. 11, pp. 3565–3583, 2006.

[14] X. He, R. G. Song, and D. J. Kong, "Microstructure and corrosion behaviour of laser-cladding Al-Ni-TiC-CeO$_2$ composite coatings on S355 offshore steel," *Journal of Alloys and Compounds*, vol. 770, pp. 771–783, 2019.

[15] M. Matula, L. Hyspecka, M. Svoboda et al., "Intergranular corrosion of AISI 316L steel," *Materials Characterization*, vol. 46, no. 2-3, pp. 203–210, 2001.

[16] J. Jiang, D. Xu, T. Xi et al., "Effects of aging time on inter-granular and pitting corrosion behavior of Cu-bearing 304L stainless steel in comparison with 304L stainless steel," *Corrosion Science*, vol. 113, pp. 46–56, 2016.

[17] C. Doerr, J.-Y. Kim, P. Singh, J. J. Wall, and L. J. Jacobs, "Evaluation of sensitization in stainless steel 304 and 304L using nonlinear Rayleigh waves," *NDT & E International*, vol. 88, pp. 17–23, 2017.

[18] P. Murkute, S. Pasebani, and O. B. Isgor, "Production of corrosion-resistant 316L stainless steel clads on carbon steel using powder bed fusion-selective laser melting," *Journal of Materials Processing Technology*, vol. 273, Article ID 116243, 2019.

[19] G. R. Argade, S. Shukla, K. Liu, and R. S. Mishra, "Friction stir lap welding of stainless steel and plain carbon steel to enhance corrosion properties," *Journal of Materials Processing Technology*, vol. 259, pp. 259–269, 2018.

[20] H. Li, L. Zhang, B. Zhang, and Q. Zhang, "Microstructure characterization and mechanical properties of stainless steel clad plate," *Materials*, vol. 12, no. 3, p. 509, 2019.

[21] S. Wang, B. X. Liu, C. X. Chen, J. H. Feng, and F. X. Yin, "Microstructure, mechanical properties and interface bonding mechanism of hot-rolled stainless steel clad plates at different rolling reduction ratios," *Journal of Alloys and Compounds*, vol. 766, pp. 517–526, 2018.

[22] Z. Dhib, N. Guermazi, M. Gaspérini, and N. Haddar, "Cladding of low-carbon steel to austenitic stainless steel by hot-roll bonding: microstructure and mechanical properties before and after welding," *Materials Science and Engineering: A*, vol. 656, pp. 130–141, 2016.

[23] ASTM A264-12(2019), *Standard Specification for Stainless Chromium-Nickel Steel-Clad Plate*, ASTM International, West Conshohocken, PA, USA, 2019.

[24] ASTM A262-15, *Standard Practices for Detecting Susceptibility to Intergranular Attack in Austenitic Stainless Steels*, ASTM International, West Conshohocken, PA, USA, 2015.

[25] Z. Dhib, N. Guermazi, A. Ktari, M. Gasperini, and N. Haddar, "Mechanical bonding properties and interfacial morphologies of austenitic stainless steel clad plates," *Materials Science and Engineering: A*, vol. 696, pp. 374–386, 2017.

[26] J. Jiang, H. Ding, Z.-M. Luo, and G.-M. Xie, "Interfacial microstructure and mechanical properties of stainless steel clad plate prepared by vacuum hot rolling," *Journal of Iron and Steel Research International*, vol. 25, no. 7, pp. 732–738, 2018.

[27] J. H. Lee, K. T. Kim, Y. S. Pyoun, and Y. S. Kim, "Intergranular corrosion mechanism of slightly-sensitized and UNSM-treated 316L stainless steel," *Corrosion Science and Technology*, vol. 15, no. 5, pp. 226–236, 2016.

[28] A. Y. Chen, W. F. Hu, D. Wang et al., "Improving the intergranular corrosion resistance of austenitic stainless steel by high density twinned structure," *Scripta Materialia*, vol. 130, pp. 264–268, 2017.

[29] K. S. Min, S. C. Lee, and S. W. Nam, "Effects of TiC and Cr$_{23}$C$_6$ carbides on creep-fatigue properties in AISI 321 stainless steel," *Materials Transactions*, vol. 43, no. 11, pp. 2808–2812, 2002.

[30] Y. Gao, C. Zhang, X. Xiong, Z. Zheng, and M. Zhu, "Intergranular corrosion susceptibility of a novel Super304H stainless steel," *Engineering Failure Analysis*, vol. 24, pp. 26–32, 2012.

[31] B. X. Liu, F. X. Yin, X. L. Dai et al., "The tensile behaviors and fracture characteristics of stainless steel clad plates with different interfacial status," *Materials Science and Engineering: A*, vol. 679, pp. 172–182, 2017.

[32] B. X. Liu, S. Wang, W. Fang, F. X. Yin, and C. X. Chen, "Meso and microscale clad interface characteristics of hot-rolled stainless steel clad plate," *Materials Characterization*, vol. 148, pp. 17–25, 2019.

[33] Y. Tao, Y.-A. Jing, Y. Xiaolin, L. Wenbin, P. Qihang, and J. Guo, "Microstructures and properties of roll-bonded stainless/medium carbon steel clad plates," *Journal of Materials Processing Technology*, vol. 266, pp. 264–273, 2019.